Experimental investigation of the wake characteristics behind twin vertical axis turbines

Stephanie Müller[a], Valentine Muhawenimana[a], Catherine Wilson[a], Pablo Ouro[b,a,*]

[a] *Hydro-environmental Research Centre, School of Engineering, Cardiff University, The Parade CF24 3AA, Cardiff, UK;*
[b] *School of Mechanical, Aerospace and Civil Engineering, University of Manchester, Manchester, M13 9PL, UK;*

Abstract

Vertical axis wind and tidal turbines are a promising technology, well suited to harness kinetic energy from highly turbulent environments such as urban areas or rivers. The power density per occupied land area of two or three vertical axis rotors deployed in close proximity can notably exceed that of their horizontal axis counterparts. Using acoustic Doppler velocimetry, the three-dimensional wake developed downstream of standalone and twin vertical axis turbines of various shaft-to-shaft distances and rotational direction combinations was characterised in terms of mean velocity and turbulence statistics, with their impact on momentum recovery quantified. Results show that the wake hydrodynamics were more impacted by turbine rotational direction than lateral distance between devices for the range of lateral spacing considered. In the cases with turbines operating in a counter-rotating forward configuration, the wake mostly expanded laterally and attained the largest velocities that exceeded those in the single turbine case, with full momentum recovery at 5 turbine diameters downstream. The wake developed by the counter-rotating backward setup notably extended over the vertical direction, whilst devices rotating in the same direction featured the greatest lateral wake expansion with reduced velocities. Linear wake superposition of the single turbine wake provided a good representation of the mean velocity field behind twin-turbine setups. The presented results indicate that, in the design of twin-turbine arrays moving in counter-rotating forward direction, a lateral spacing of, at least, two turbine diameters should be kept as this allows the kinetic energy in the wake to be fully recovered by five turbine diameters downstream.

*Corresponding author
Email address: `pablo.ouro@manchester.ac.uk` (Pablo Ouro)

Keywords: vertical axis turbine, VAWT, wakes, river turbine, turbine array, turbulence

1. Introduction

The continuous increase in energy demand and current change in energy policy towards net-zero carbon economies is leading to the rapid expansion and development of new sustainable renewable energy technologies. To date, hydropower is the second-largest source of renewable energy [1] and has long been considered as an environmentally friendly and clean form of energy generation. However, the growing concern about the ecological impact of traditional large-scale hydropower projects [2] is propelling the development of small-scale, low-head hydro-kinetic alternatives [3], e.g. horizontal (HAT) and vertical (VAT) axis river turbines.

There has been an increased interest by the research community to improve the design of VATs, both to enhance the rotor's efficiency and deploy VATs in arrays to take advantage of flow acceleration due to blockage effects of closely located turbine rotors [4] that increase by 10 times the installed power capacity of HATs [5]. VATs offer a wide range of mechanical and hydrodynamic advantages compared to HATs. Their vertical rotational axis, for instance, allows positioning of the generator and other heavy components on the ground or a floating platform, which diminishes their technical complexity compared to HATs and improves their suitability to river applications [6]. From an operational point of view, the relatively low rotational speed and rectangular cross-section that maximise the swept rotor area in constrained shallow waters make them particularly suitable for rivers and estuaries with low-to-medium flow velocities [6]. VATs operate independently of the flow direction, i.e. they are omnidirectional; hence, no yaw-angle correction and alignment with the flow direction is needed. Subsequently, these unique operational characteristics also have the advantage of potentially reducing the environmental impact by operating at lower rotational speed than HATs. This, in turn, lowers acoustic contamination [6] and presents a potential reason for the lack of injuries and mortality observed for VATs [7]. Despite this promising catalogue of benefits, VAT's main drawback remains their lower performance compared to HATs, however this can be overcome if several VAT rotors are deployed in close proximity as an array [8].

The wake developed by a single VAT has been extensively studied through small-scale experimental testing in open channels (such as those from Brochier et al. [9], Bachant and Wosnik [10], Araya et al. [11], Ouro et al. [12] or Strom et al. [13]), wind tunnels (e.g. studies from Tescione et al. [14], Kadum et al. [15], Rolin and Porté-Agel [16] or Vergaerde et al. [17]), and high-fidelity numerical simulations

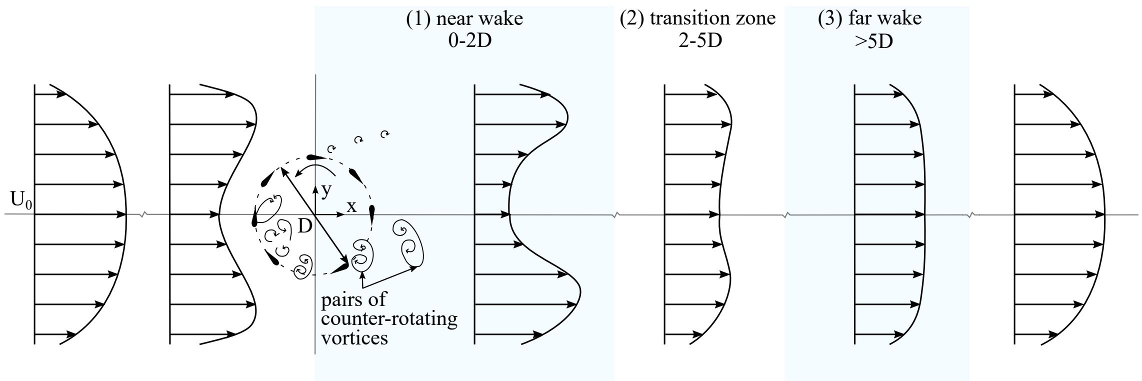

Figure 1: Wake evolution of a single, counter-clockwise rotating VAT of diameter D, consisting of three distinct regions: (1) a near-wake region ($x/D \leq 2$), characterised by a low-momentum region laterally bounded by shear layers that result from the advection of two pairs of counter-rotating vortices over the downstroke side and smaller vortices over the upstroke side; (2) a transition zone ($2 \leq x/D \leq 5$); and (3) a far-wake region ($x/D \geq 5$) characterised by wake recovery.

(including the work from Shamsoddin and Porté-Agel [18], Lam and Peng [19], Posa et al. [20], Abkar and Dabiri [21], Ouro and Stoesser [22], or Posa [23]). Only a handful of full-scale devices have been tested in field campaigns, e.g. in a wind turbine array [8] or in a tidal flow [24].

Based on the observations from these studies, the primary regions developed in the wake of a VAT in an open-channel are depicted in the schematic presented in Figure 1, which outlines three distinct regions, namely the near-wake ($x/D \leq 2$), transition zone ($2 \leq x/D \leq 5$), and far-wake ($x/D \geq 5$) [12], with x indicating the streamwise location and D being the turbine diameter. The near-wake region is characterised by the turbine-induced flow structures such as the two counter-rotating vortices shed by the blades when undergoing dynamic stall during the downstroke phase [9]. The latter coherent turbulent structures generate a shear layer that isolates the low-momentum region developed in the near-wake core from the high-velocity region outside the wake, thus limiting entrainment of the surrounding flow [12]. The blades experience lower flow separation over the upstroke rotation as their relative velocity is larger than during their downstroke motion, which also prevents deep dynamic stall [22]. The shedding pattern of these turbulent structures depends on the tip-speed ratio, i.e., the relative blade velocity to that of the approaching flow. This unevenly generated flow during the downstroke and upstroke motion of the rotor blades can render the near-wake asymmetric about its centreline [14]. Within the transition zone, the wake starts to vertically and laterally expand with a larger ambient turbulent flow entrainment that increases the turbulent fluxes and intensity, and momentum begins to recover at a faster rate [12]. In the far-wake region, the core momentum further recovers with increasing downstream distance until it eventually reaches a mean velocity value similar to that of the free stream flow at distances that vary with the turbine's aspect ratio [25] and dynamic solidity [11].

2. Problem statement

To unfold the full potential of VATs, there remains a need for a detailed understanding of wake hydrodynamics of multiple VATs in order to identify their optimal arrangement and thus maximise the harnessed kinetic energy when deployed in arrays [26]. The pilot wind-energy project FLOWE [8], for instance, showed that VATs could achieve a higher power density than HATs when deployed in twin configurations. To date, VAT wake interactions have been studied mostly for side-by-side twin-turbine setups, mainly focusing on the turbines' rotational direction with numerical simulations [27] and wind tunnel testing [17] and less on the shaft-to-shaft lateral spacing and relative alignment to the incident flow direction [28].

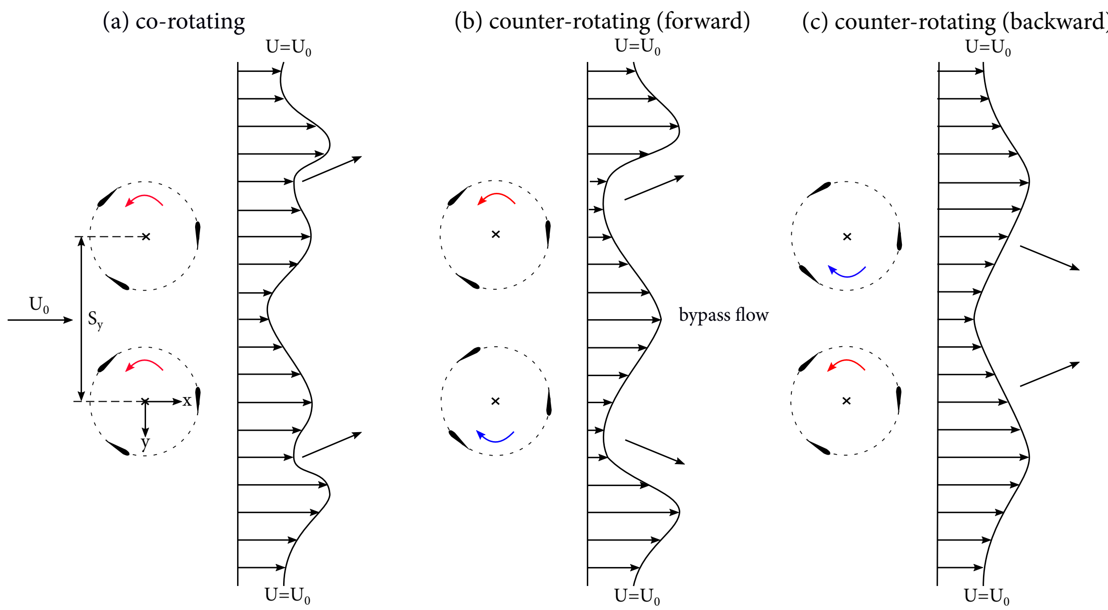

Figure 2: Wake interaction of three twin-VAT arrangements varying in rotational direction, laterally spaced by S_y, namely (a) co-rotating, (b) counter-rotating forwards, and (c) counter-rotating backwards.

Figure 2 depicts twin-VAT setups with devices co-rotating or counter-rotating forward and backward, corresponding to cases in which blades move with or against the flow direction in the bypass region. Comparison of the wake evolution for these configurations shows that the individual wakes of co-rotating VATs (Figure 2a) evolve independently in the downstream direction, with a reduced interference in the near-wake [29]. These wakes start to interact with each other and partially merge at a downstream distance that depends on the relative shaft-to-shaft separation (S_y/D) [27]. The individual wakes of two turbines in the counter-rotating forward configuration (Figure 2b), on the other hand, spread outwards in an axisymmetric fashion, leading to laterally expanded wakes that progressively diverge with increasing downstream distance and creating high momentum flow region between both turbines. Conversely, in the counter-rotating backward case, a prolonged combined wake is observed after the transition zone. Both individual wakes progressively move towards each other before merging and interacting [29]. This results in a lower high-velocity bypass region [27] that varies with both turbine rotational direction and intra-turbine spacing, i.e. smaller S_y/D values result in a higher flow blockage within the bypass region that reduces the flow velocity in this area.

The wake patterns observed for twin-VATs have been mostly characterised in the horizontal plane by two-dimensional simulations to study rotor position [30] and intermediate deflector influence [31] with limited experimental and numerical in-depth studies looking at the three-dimensional wake evolution for multi-turbine arrangements. In this paper, the three-dimensional wake hydrodynamics behind a single turbine, and co- and counter-rotating twin-turbine setups are experimentally investigated using acoustic Doppler velocimetry measurements, and the impact of six different lateral spacing and rotational direction combinations on the wake characteristics are quantified. The paper is structured as follows: Section 3 describes the experimental facility and techniques used, along with the turbine design and configurations tested. Section 4 presents the mean velocity and turbulence statistics, cross-averaged values of velocity and turbulence intensity over the measured wake length for the single turbine and twin-VAT cases, and linear and quadratic wake superposition is applied to predict twin-VAT wake dynamics. Conclusions are drawn in Section 5.

3. Methods

Details of the experimental facility in which the tests were performed, turbine rotor dimensions and operation, and the flow measurement method are provided in this section.

3.1. Flume setup

The experiments were conducted in the Hydro-environmental Research Centre's hydraulic laboratory at Cardiff University, UK. The experimental setup, depicted in Figure 3, used a 10m long, 1.2m wide, and 0.3m deep recirculating flume with a slope of 0.001. Flow depth and discharge were controlled by a pump and a tailgate weir which were located at the downstream end of the flume and kept constant throughout the experiment. Flow depth was measured using a Vernier pointer gauge with an accuracy of $\pm$0.1mm while discharge was measured with an ultrasonic flowmeter (TecFluid Nixon CU100) with a precision of $\pm$1.5%. Prior to rotating the VAT in each of the tests, sub-critical uniform flow with a discharge of $Q = 0.053\text{m}^3\text{s}^{-1}$ and a flow depth of $h_0 = 0.23$m were established. Further hydraulic parameters are presented in Table 1, including cross-section averaged bulk velocity $U_0 = Q/A$, bulk Reynolds number ($Re = U_0 R_H/\nu$ with ν denoting the fluid kinetic viscosity and R_H the hydraulic radius), Reynolds number based on turbine diameter D ($Re_D = U_0 D/\nu$), and Froude number ($Fr = U_0/\sqrt{gh_0}$).

Table 1: Details of hydraulic parameters adopted in the experiments, including flow discharge (Q), water depth (h_0), bulk velocity (U_0), bulk Reynolds number (Re), Reynolds number based on the turbine's rotor diameter (Re_D), and Froude number (Fr).

Q	h_0	U_0	Re	Re$_D$	Fr
[m^3s^{-1}]	[m]	[ms^{-1}]	[-]	[-]	[-]
0.0053	0.23	0.19	$3.16 \cdot 10^4$	$2.28 \cdot 10^4$	0.13

3.2. Description of the VATs

The adopted VATs were manufactured with a rotor diameter $D = 0.12$m and height $H = 0.12$m, i.e. with an aspect ratio H/D equal to unity. The rotor comprised three blades ($N_b = 3$) that were 3D printed with laser-sintered PA 2200 material conforming to a NACA 0015 airfoil profile geometry with zero preset pitch angle and 0.03m chord length (c), which yielded a geometric solidity $\sigma = N_b c/\pi D \approx 0.24$. DC motors (Nider DMN37K50G18A, DC 12V) were used in each turbine to impose a constant rotational speed $\Omega = 59$rpm for an optimum tip-speed ratio $\lambda = 1.9$ [12]. Each blade was attached to a main circular shaft of 0.006m diameter using two horizontal struts of 0.003m diameter, attached at vertical positions 0.01m away from the bottom and top tips of the blades; both components were made of stainless steel. The bottom end of the turbine shaft was connected to a bearing attached to the flume bed, leaving a clearance of 0.02m to the bottom tip of the blades. The

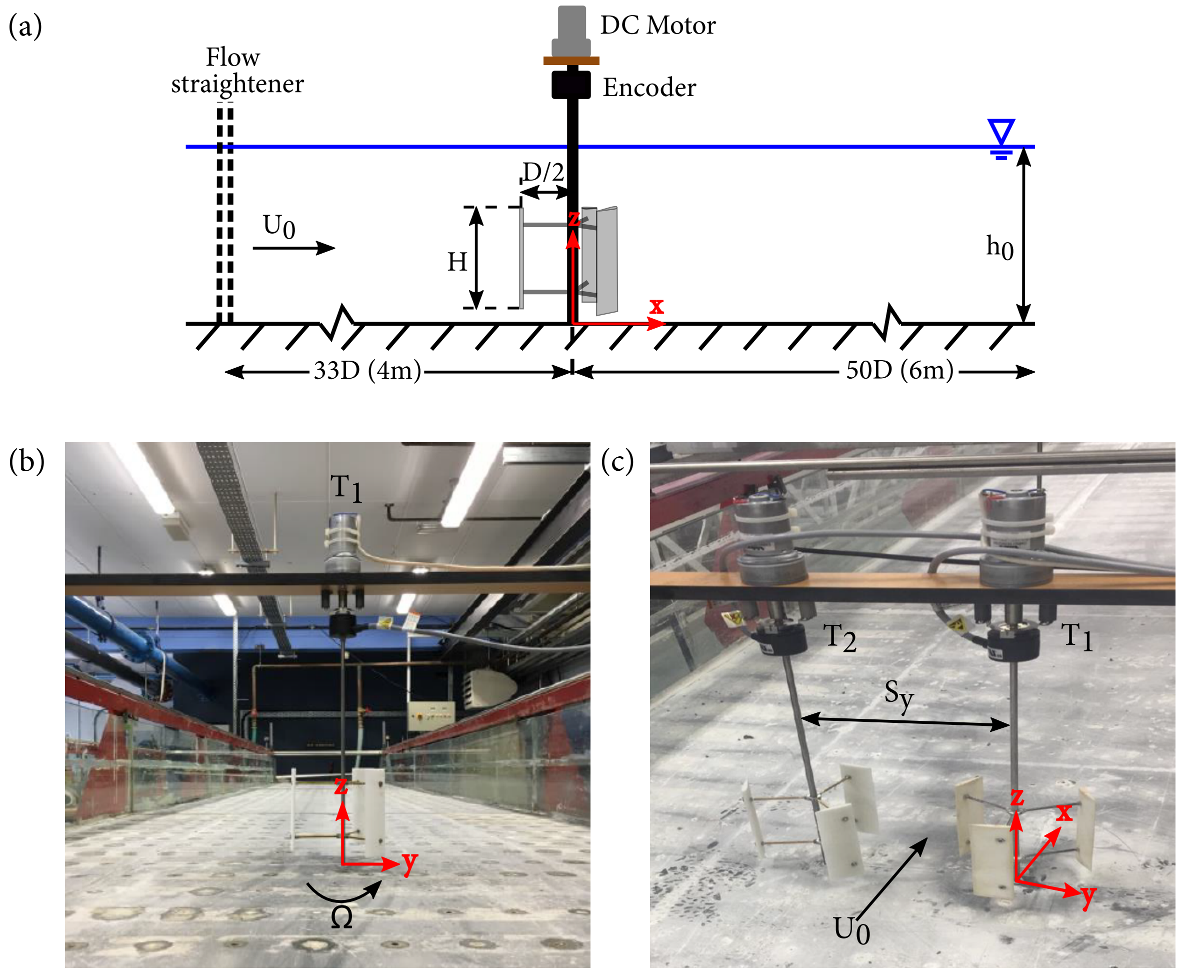

Figure 3: (a) Schematic of the experimental setup, depicting the streamwise location of a single VAT of height H and radius $D/2$, (b) photograph of the VAT T_1 located at the flume centre, $33D$ downstream of the flume inlet and rotating in counter-clockwise direction, (c) photograph of twin-VAT setup comprising of VATs T_1 and T_2 laterally spaced by a distance of S_y.

upper end of the shaft was connected to an encoder (Kübler, 5-30VDC, 100mA) that measured the rotational speed.

The first turbine, T_1, was placed at the centre of the flume cross-section as shown in Figure 3 at a distance of 4m downstream of the flume inlet. The position of T_1 was set as the coordinate origins, considering as positive x-coordinates the streamwise flow direction, the positive lateral (y) direction over the right-hand side of the flume, and the z-coordinates in the upward direction starting at the flume's bed. In the array

Table 2: Details of the single and twin-turbine configurations test cases, including rotational direction and lateral spacing between turbines (S_y).

Test case	Description	Direction of rotation	S_y/D
ST	Single turbine	T_1 anti-clockwise	-
SR–1.5	Same rotation	T_1 and T_2 anti-clockwise	1.5
CRF–1.5	Counter-rotating forward	T_1 clockwise and T_2 anticlockwise	1.5
CRB–1.5	Counter-rotating backward	T_1 anti-clockwise and T_2 clockwise	1.5
SR–2.0	Same rotation	T_1 and T_2 anti-clockwise	2.0
CRF–2.0	Counter-rotating forward	T_1 clockwise and T_2 anticlockwise	2.0
CRB–2.0	Counter-rotating backward	T_1 anti-clockwise and T_2 clockwise	2.0

configurations, the second turbine T_2 was placed at the same streamwise location with a lateral shaft-to-shaft separation of S_y, as indicated in Figure 4.

A total of six twin-turbine configurations were tested, whose details, including turbine rotational direction and intra-spacing, are summarised in Table 2. First, a single, counter-clockwise rotating turbine (Figure 3b) was tested to characterise an individual VAT wake to be used as a reference wake distribution for the twin-turbine wake analysis. In the twin configurations, two shaft-to-shaft intra-turbine spacings, S_y of $1.5D$ and $2.0D$, were considered, in combination with the different rotational directions for each turbine, as depicted in Figure 2. The co-rotating case (hereinafter denoted as "same rotation" SR setup) considered both VATs to move with counter-clockwise motion (Figure 2 (a)). Then, two scenarios with turbines rotating in opposite directions, namely counter-rotating setups, were tested. These include the (1) "counter-rotating forward" CRF setup (Figure 2 (b)) in which the blades moved in the flow direction in-between rotors (i.e., in the bypass flow region); and (2) the "counter-rotating backward" CRB setup in which blades travelled against the incident flow in this region (Figure 2 (c)). For instance, the setup CRF–1.5 denotes the counter-rotating forward layout with an inter-turbine separation of $1.5D$.

3.3. Hydrodynamic measurements

Hydrodynamic measurements were conducted using a side-looking Acoustic Doppler Velocimeter (ADV) (Nortek Vectrino). To ensure sufficient data quality and capture of a representative sample of the high-frequency turbulence fluctuations characteristic from VAT wakes, sampling periods of 300s (cross-sections at $x/D = 1.0$, 1.5 and 2.0) and 180s (cross-sections at $x/D > 2.0$) were adopted with a frequency of 200Hz. Signal quality was enhanced by seeding the water with Sphericel® 110P8 hollow glass spheres (Potters Industries LLC) with a mean particle size 11.7μm and specific gravity of 1.10g/cc.

To characterise the approach flow conditions, one lateral cross-section was measured at 1m upstream of the turbine (approx. $8D$). This cross-section comprised six vertical velocity profiles laterally spaced by 0.1m, starting at $y/D = 0$. Each velocity profile consisted of 20 measurement points vertically spaced by $\Delta z = 0.01$m ($0.08D$), starting at 0.01m above the flume bed until approx. 0.03m below the water surface. Then, for each of the single and twin-turbine configurations, lateral cross-sections ($y - z$ planes) were measured at nine streamwise locations starting at $1D$ and reaching until $10D$ downstream of the turbine, as depicted in Figure 4 (a). Each cross-section comprised 12 to 14 vertical velocity profiles in the lateral direction for the single and twin-turbine setups, respectively. Lateral spacing between vertical profiles was 0.05m ($0.42D$) (ST: $-1.25 \leq y/D \leq 1.25$, twin-VATs: $-1.25 \leq y/D \leq 7.92$), and increased to 0.1m ($0.83D$) within the free-stream region, as shown in Figure 4 (b).

Velocity data were filtered and post-processed using Matlab (2019a). Data with SNR $\leq$ 15% and COR $\leq 70dB$ were removed from the data set, after which data were despiked using an open-source toolbox [32] provided in [33]. The instantaneous filtered velocity vector $\boldsymbol{u} = (u, v, w)$ record was then divided using the Reynolds decomposition: $\boldsymbol{u}(t) = \overline{\boldsymbol{u}} + \boldsymbol{u}'(t)$, with the time-averaged operation denoted as $\overline{(\cdot)}$ and the fluctuating components represented as $(\cdot)'$. Normalised turbulence statistics were computed in terms of streamwise turbulence intensity ($u'/U_0 = \sqrt{\overline{u'u'}}/U_0$), turbulent kinetic energy ($tke = 0.5(\overline{u'u'} + \overline{v'v'} + \overline{w'w'})/U_0^2$), and Reynolds shear stresses ($\overline{u'v'}/U_0^2$ and $\overline{u'w'}/U_0^2$). Cross-sectional plots are presented normal to the flow and looking in the downstream flow direction.

4. Results and Discussion

In this section, the ADV measurements that characterise the approach flow and the wake behind the single and twin-turbine configurations are presented. Further analysis is provided in terms of downstream evolution of the spatially-averaged wake velocity and wake superposition techniques.

4.1. Approach flow

The vertical distribution of normalised streamwise mean velocity ($\overline{u}/U_0$), streamwise turbulence intensity (u'/U_0), and vertical Reynolds shear stresses ($\overline{u'w'}/U_0^2$) are presented in Figure 5 (a-c), respectively, for six lateral locations over the left half of the cross-section (the approach flow is deemed symmetric). The mean velocity profiles show a power-law distribution over the flow depth, with a nearly constant turbulence intensity distribution yielding a depth-averaged value of $u'/U_0 = 0.14$.

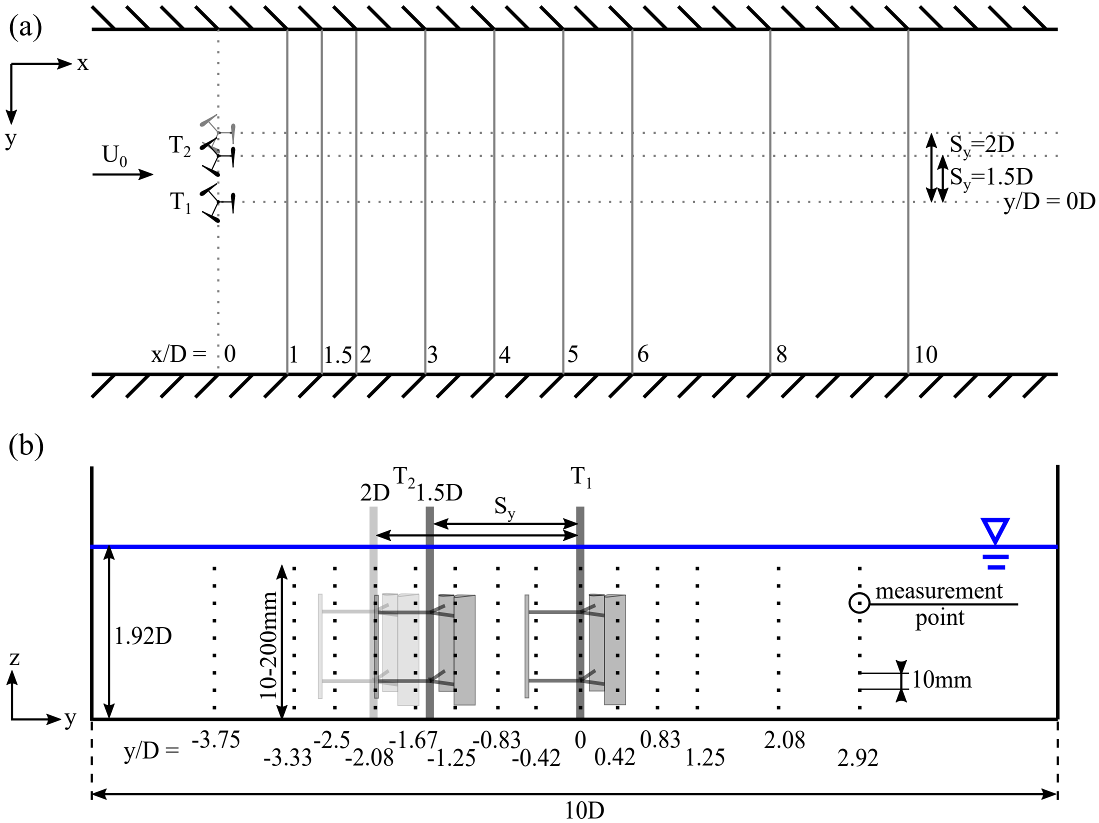

Figure 4: ADV wake measurement locations, showing (a) locations of cross-sections ($y - z$ plane) measured in streamwise direction, starting at $1D$ and until $10D$ downstream of the turbines, and (b) lateral distribution of the vertical measurement profiles over the flume section.

There is some non-uniformity in the $u'w'$ distribution between lateral locations, especially at $y/D =$ -4.17, attributed to its proximity to the flume wall (located $0.83D$ away from the lateral wall), which can impact the distribution of turbulent fluxes [34].

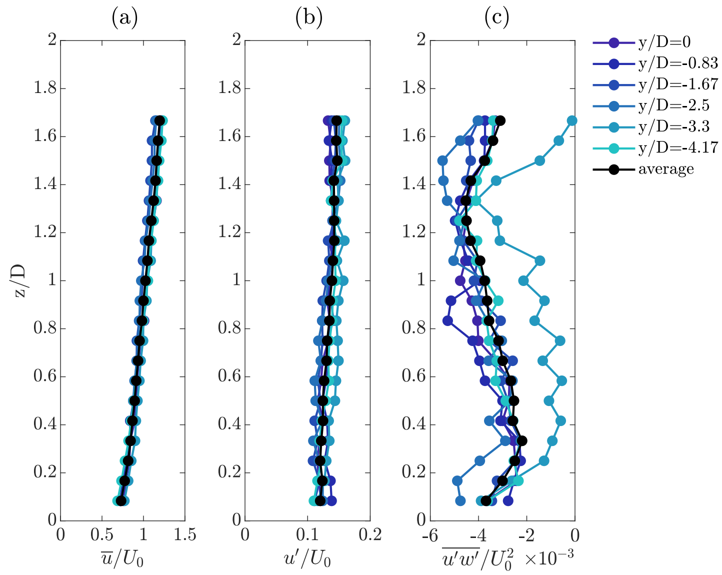

Figure 5: Upstream profiles measured at six lateral locations beginning at the flume centreline ($y/D = 0$). (a) Time-averaged streamwise velocity $\overline{u}$ normalised by the bulk velocity U_0, (b) streamwise turbulence intensity u' normalised by U_0, and (c) vertical Reynolds shear stress $\overline{u'w'}$ normalised by U_0^2. The black line and symbols correspond to the average value from the vertical measurements.

4.2. Single turbine wake evolution

Before examining the dynamics of twin-turbine wakes, the wake characteristics of the single turbine (ST) case are presented in $y-z$-planes at downstream distances (x/D) from one to five diameters to identify its key characteristics and three-dimensional evolution. The black rectangular outline in the contour plots represents the projected area of the turbine's rotor (see Figure 6).

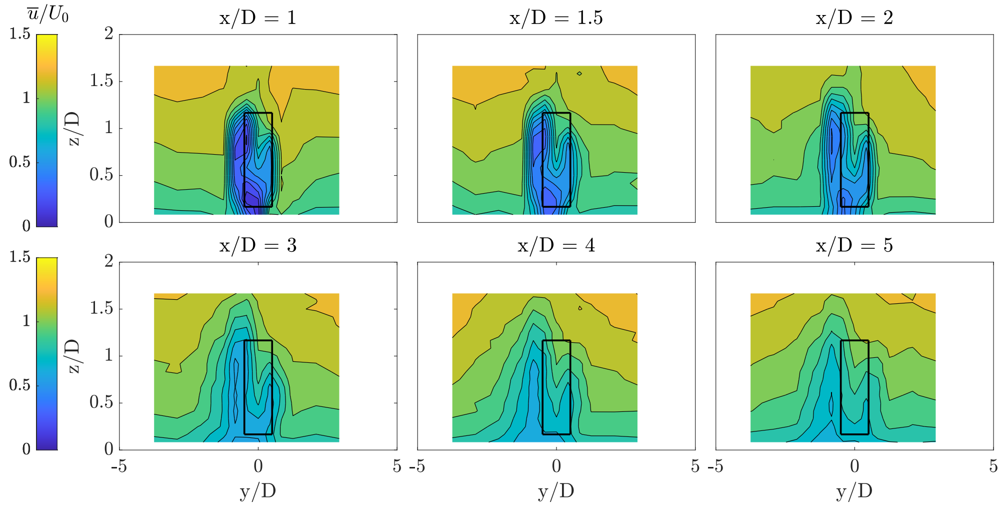

Figure 6: Contours of $\overline{u}/U_0$ at downstream cross sections located at $x/D = 1$, 1.5, 2, 3, 4 and 5 for the case with the single turbine (ST) rotating with anti-clockwise motion. The solid black rectangle represents the perimeter of the turbine's rotor. Flume's centreline is at $y/D = 0$.

The distribution of the normalised mean streamwise velocity ($\overline{u}/U_0$) is shown in Figure 6. The near wake ($x/D \leq 2$) behind the ST was characterised by a region of large velocity deficit immediately downstream of the rotor, which was particularly pronounced on the upstroke part ($y/D \leq 0$) of the blades' rotation, i.e., when the blades move against the flow thus generating the highest relative velocity. This causes the wake to be asymmetric relative to the rotor centreline which has previously been observed by [9]. Until $x/D = 2$, the areas near the top and bottom tips in the upstroke side appeared to attain the minimum velocity values, likely arising from tip-vortices generated by the blades, similar to the PIV results presented in [16]. Over the downstroke side ($y/D \geq 0$) the velocity was larger, with the lowest values distributed over the mid turbine height ($0.3 \leq z/D \leq 0.9$) rather than the tip location. Beyond $x/D = 3$, the transitional-wake region [12] was characterised by a vertical and lateral expansion of the low-velocity wake. In the far wake ($x/D \geq 6$, not shown here for brevity) most of the momentum was recovered, with velocities yielding values close to the approach flow velocity, but remnants of the wake signature were still visible over the whole water column. Overall, the wake evolution observed for the ST case is similar to the wake previously outlined in Figure 1, and those presented in [16] whose Reynolds number was almost one order of magnitude higher.

The distribution of turbulent kinetic energy (tke) is presented in Figure 7. Similar to the distribution of $\overline{u}/U_0$, the upstroke side over the whole wake length featured

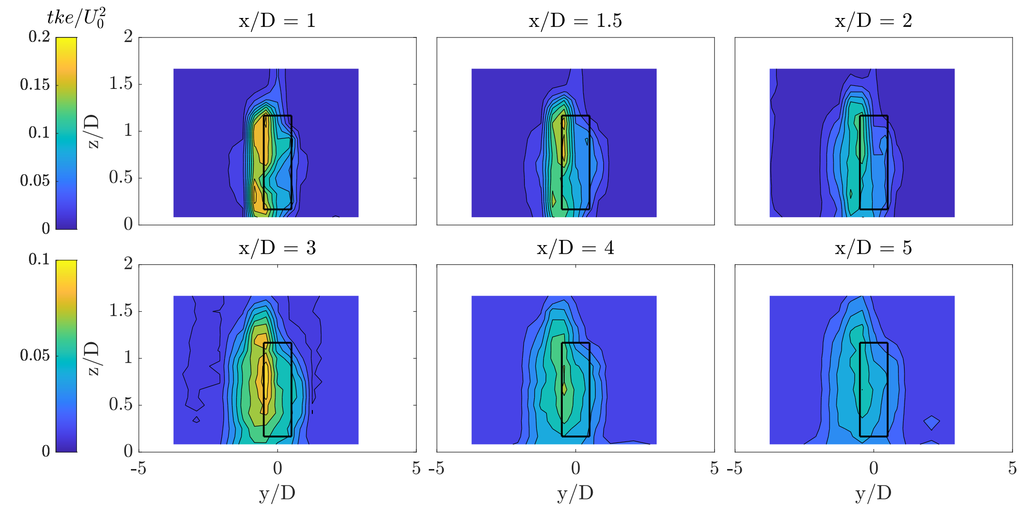

Figure 7: Contours of tke/U_0^2 at downstream cross sections located at $x/D = 1$, 1.5, 2, 3, 4 and 5 for the ST case, with the VAT rotating anti-clockwise. The solid black rectangle represents the perimeter of the turbine's rotor. Flume's centreline is at $y/D = 0$. Note that the range of values is adjusted for each row of contours corresponding at different streamwise locations.

the highest values of tke due to the turbine blades moving into the flow and energetic vortices being generated and shed [22]. Over the downstroke side, turbulence levels were significantly lower, likely linked to the reduced dynamic-stall vortices strength due to the Reynolds number of the experiments.

Turbulent momentum exchange is indicated by the horizontal and vertical components of the Reynolds shear stress ($\overline{u'v'}/U_0^2$, Figure 8, and $\overline{u'w'}/U_0^2$, Figure 9, respectively), which shows that regions of highest shear stresses were mostly found in the near wake. The high magnitudes observed for $\overline{u'v'}$, originated from the convection of dynamic-stall vortices and interaction with the ambient flow, included both positive and negative values on the upstroke side ($y/D \leq 0$), with the latter found on the outside region of the turbine's rotor swept area and the former $u'v'$ inside it. This pattern was observed only over the near-wake region as the turbine-induced vortical structures lose their coherence due to the mixing with the ambient flow.

Vertical Reynolds shear stresses ($\overline{u'w'}/U_0^2$) showed predominantly negative values on the upper half of the turbine ($z/D \geq 0.8$), due to the flow over-topping the turbine being transported downward into the wake. In the near wake ($x/D \leq 2$), positive $\overline{u'w'}$ values appeared on the lower half of the turbine ($z/D \leq 0.7$) with particularly large values near the corners of the rotor's swept area, which unveils the interaction

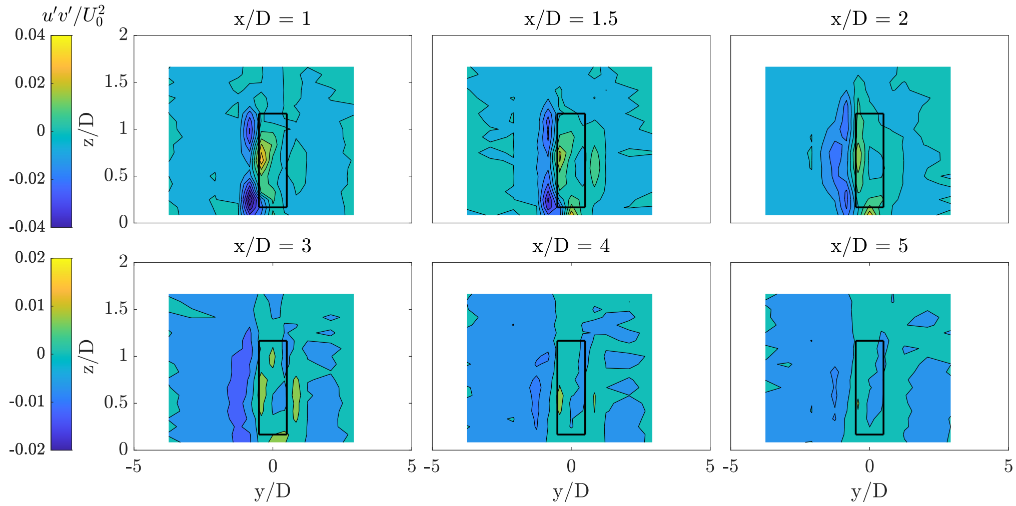

Figure 8: Contours of $\overline{u'v'}/U_0^2$ at downstream cross sections located at x/D = 1, 1.5, 2, 3, 4 and 5 for the ST case, with the VAT rotating anti-clockwise. The solid black rectangle represents the perimeter of the turbine's rotor. Flume's centreline is at $y/D = 0$. Note that the range of values is adjusted for each row of contours corresponding at different streamwise locations.

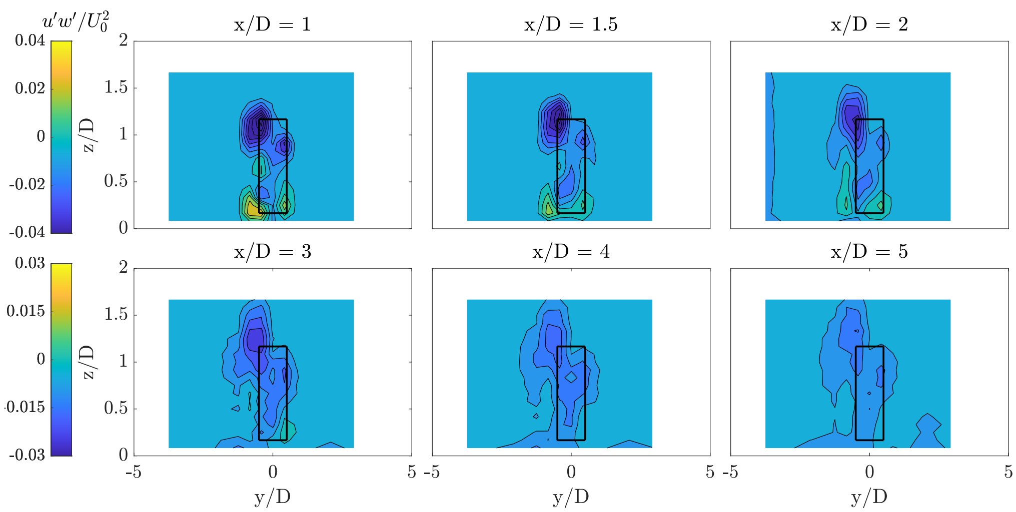

Figure 9: Cross section contours of $\overline{u'w'}/U_0^2$ at downstream locations of x/D = 1, 1.5, 2, 3, 4 and 5 for the ST case, with the VAT rotating anti-clockwise. The solid black rectangle represents the perimeter of the turbine's rotor. Flume's centreline is at $y/D = 0$. Note that the range of values is adjusted for each row of contours corresponding at different streamwise locations.

between the bottom tip vortices and the upward flow going through the bottom gap between the turbine's rotor and flume bed. Further downstream after $x/D = 3$ again, $\overline{u'w'}$ shear stresses have significantly decayed due to the mixing of the wake with the ambient flow.

4.3. Twin-VAT wake results

The impact of rotational direction and lateral turbine spacing is now elucidated for each of the twin-VAT cases. The characteristics of the wakes developed downstream of the six twin-VAT setups, i.e., for three rotation combinations and two inter-turbine spacings: SR–1.5, CRF–1.5, CRB–1.5, SR–2.0, CRF–2.0, and CRB–2.0, were analysed using contours at cross-sections normal to the flow direction ($y - z$-planes) at several streamwise locations. Mean streamwise velocities are presented for cases adopting the two inter-turbine separations of $S_y/D = 1.5$ and 2.0 while higher-order statistics are discussed only for setups with $S_y/D = 1.5$, as those with $S_y/D = 2.0$ have a similar spatial distribution and for brevity are included in the Appendix (Section 6).

Contours of $\overline{u}/U_0$ at $x/D = 1$, 2, 3, 5 and 10 are presented in Figure 10 for SR–1.5, CRF–1.5, and CRB–1.5, and in Figure 11 for SR–2.0, CRF–2.0, and CRB–2.0. Similar wake characteristics to the ST case (Figure 6) were found in individual wakes at $x/D = 1.0$ behind each of the turbines for the SR and CRF cases, with the lowest velocities found on the upstroke side of the blades rotation [17]. For CRF–1.5, the wakes appear asymmetric to the vertical axis between the turbines. However, in the CRB–1.5 case the wakes already merge at $x/D = 1.0$, as the low-momentum region of the individual wakes collapse.

In the SR–1.5 and SR–2.0 cases, the same rotational direction of both turbines caused the individual asymmetric wakes to progress alongside each other within the near-wake ($x/D \leq 2$), which is better depicted from the setup with $S_y/D = 2.0$. In the transition zone ($x/D \geq 2$) both wakes started to interact and merge into a single combined low-momentum region by $x/D = 5$, as represented in Figure 2 (a) and similar to [29]. In the far-wake, the velocities show that the combined wake expanded vertically across the water column and laterally, especially to the left-hand side of T_2. In fact, the widest wake extent was found at $x/D = 10.0$ for this configuration.

The individual wakes in the CRF (counter-rotating forward) cases move outwards in opposite directions [17], with the bypass flow enhanced by the downstroke rotation of the blades which further separated both low-momentum wakes, especially for the CRF–2.0 setup, as illustrated in Figure 2 (b). Both wakes remained separated by the bypass flow until $x/D \approx 1.5$ and mirrored each other relative to the centreline

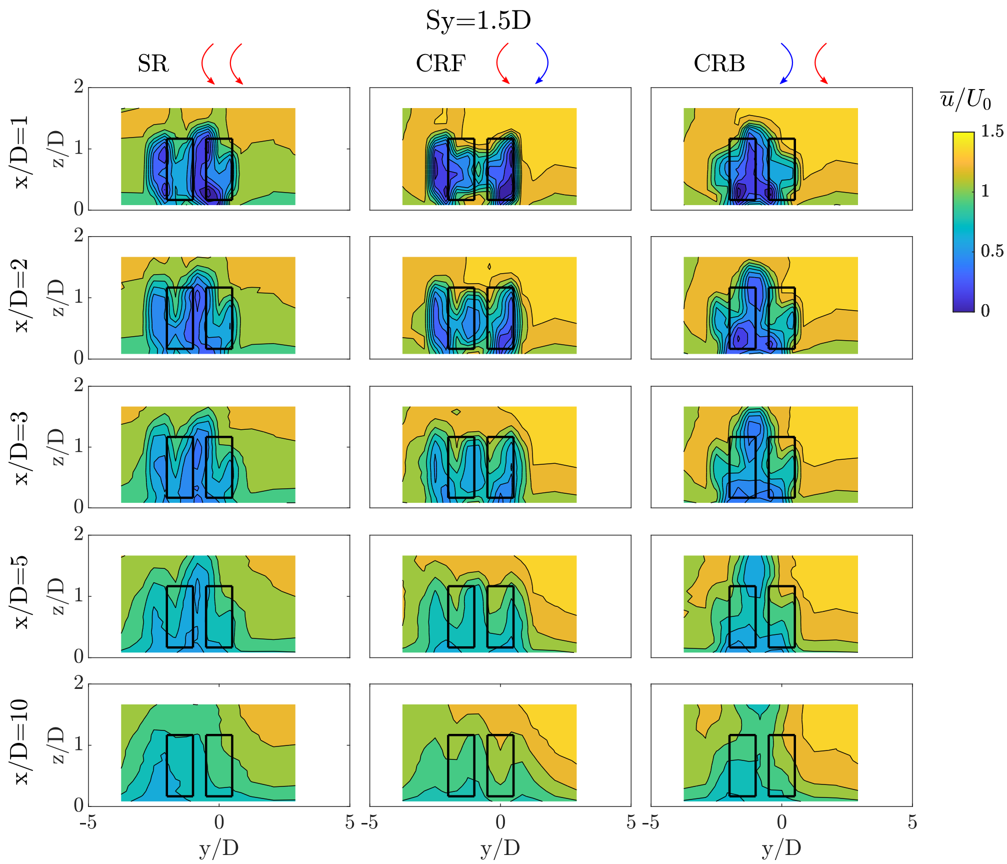

Figure 10: Cross section contours of $\overline{u}/U_0$ at downstream locations of x/D = 1, 2, 3, 5 and 10 for the SR–1.5 (left), CRF–1.5 (middle), and CRB–1.5 (right) cases. The solid black rectangles represent the perimeter of the turbine's rotor and the flume's centreline is located at $y/D = 0$.

through the gap spacing S_y. For CRF–1.5, the wakes gradually merged with further increasing downstream distance ($x/D \geq 5$), although for CRF–2.0 these appear to be more independent, likely due to the blades' downstroke motion within the bypass region that further amplified the relative velocity of the flow through, i.e., $\overline{u}/U_0 \geq 1$, thus isolating both wakes and delaying their mixing. Similarly, [17] observed that both wakes were separated by the bypass flow until $x/D \approx 6$ for CRF twin-turbines spaced by $S_y/D = 1.2$, which is in agreement with the presented results for the CRF–1.5 case. For an inter-turbine spacing of $S_y/D = 2.0$, [29] reported almost no interaction between both wakes by $x/D = 10$ as observed in this study. The region of limited interaction between both turbine wakes suggests an ideal location

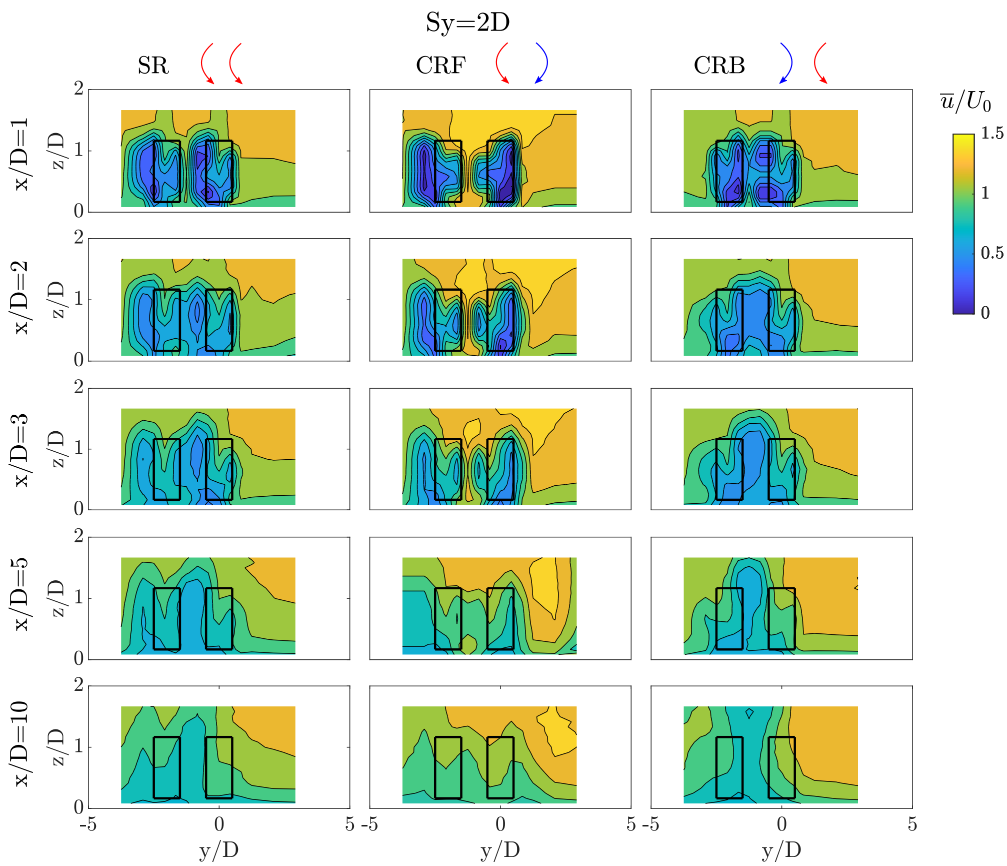

Figure 11: Cross section contours of $\overline{u}/U_0$ at downstream locations of x/D = 1, 2, 3, 5 and 10 for the SR–2.0 (left), CRF–2.0 (middle), and CRB–2.0 (right) cases. The solid black rectangles represent the perimeter of the turbine's rotor and the flume's centreline is located at $y/D = 0$.

for positioning a second row of turbines downstream.

Such limited interaction led to the wake in the CRF cases having the highest streamwise velocities at the furthest measured location of $x/D = 10$ compared to the other setups, as shown later in Section 4.4 in terms of spatially averaged velocity values.

In the CRB (counter-rotating backward) cases, individual turbine wakes interacted with one another shortly downstream of the rotors, collapsing into a single low-momentum region at $x/D = 1.0$ for the CRB–1.5 case whilst two wakes were observed for CRB–2.0 at $x/D = 1.0$ which merged at $x/D = 2.0$. Similarly, in [29] wakes began to merge at $x/D = 3.0$ and completely merged by $x/D = 7.0$ for a sim-

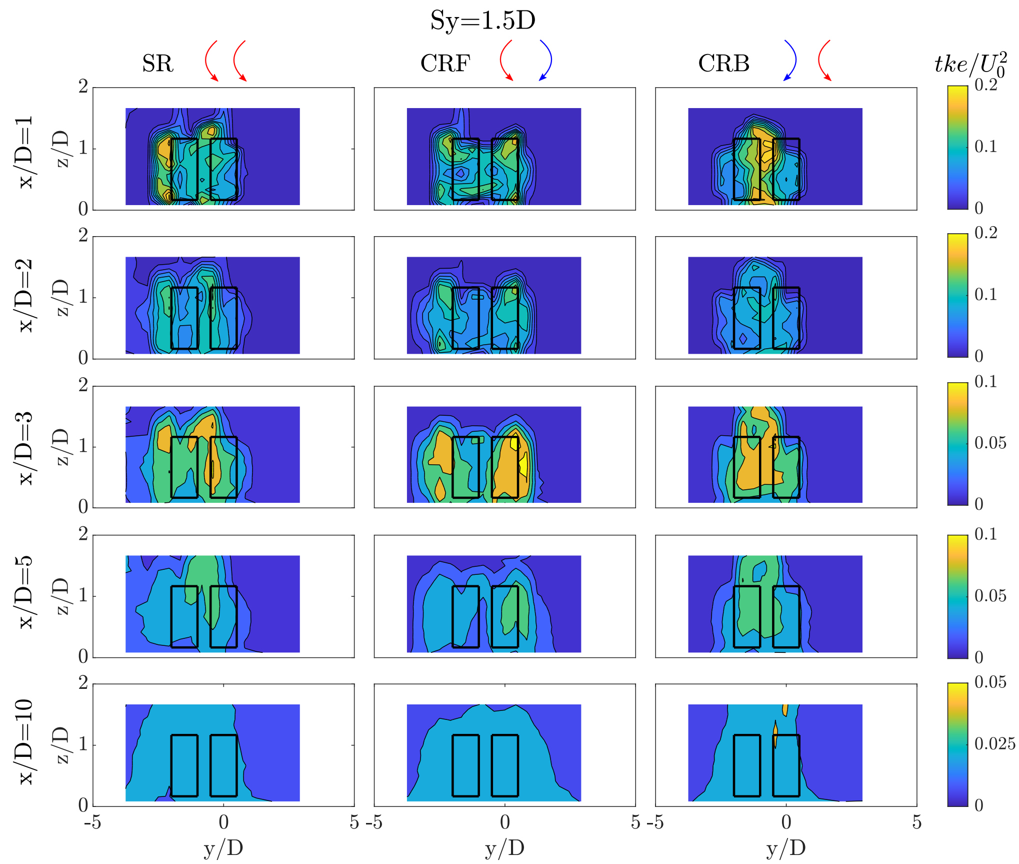

Figure 12: Cross section contours of tke/U_0^2 at downstream locations of x/D = 1, 2, 3, 5 and 10 for the SR–1.5 (left), CRF–1.5 (middle), and CRB–1.5 (right) cases. The solid black rectangles represent the perimeter of the turbine's rotor. The flume's centreline is located at $y/D = 0$. Legend scale is adjusted at every streamwise location (x/D) to ease depiction of hydrodynamic features.

ilar CRB–2.0 case. Such collapse into a single wake resulted from a weaker bypass flow as in this region the blades moved into the flow (upstroke rotation) [29]. After $x/D = 3.0$, the combined wake occupied a narrower lateral extent compared to SR and CRF cases, extended notably in the vertical direction throughout most of the water column, and was nearly axisymmetric relative to the vertical axis at the centre of the combined swept area, i.e., $S_y/2$.

The distribution of tke/U_0^2 (Figure 12) for each of the $S_y/D = 1.5$ configurations was found to be similar to that for the ST case (Figure 7), i.e. the areas with highest tke pockets are those with the lowest velocity magnitude. During the upstroke movement, the blades shed vortical structures that increased turbulent mixing and triggered high levels of tke/U_0^2. Although both wakes in the SR–1.5 case evolve independently in the near-wake region, their interaction and merging in the transition zone ($x/D \geq 2$) resulted in a region of high turbulent kinetic energy behind the twin-turbine swept area, which enhanced the mixing of both wakes [29]. Particularly high values of tke/U_0^2 were observed in the bypass region immediately downstream of the CRB–1.5 case due to the collapse of the wake regions generated from the upstroke motion of the blades. In this region, the tke values for CRF–1.5 were reduced, with maxima located on the outskirts of the wake. With increasing downstream distance, the turbulent kinetic energy decreased to approach the values of the upstream tke levels at $x/D = 10$.

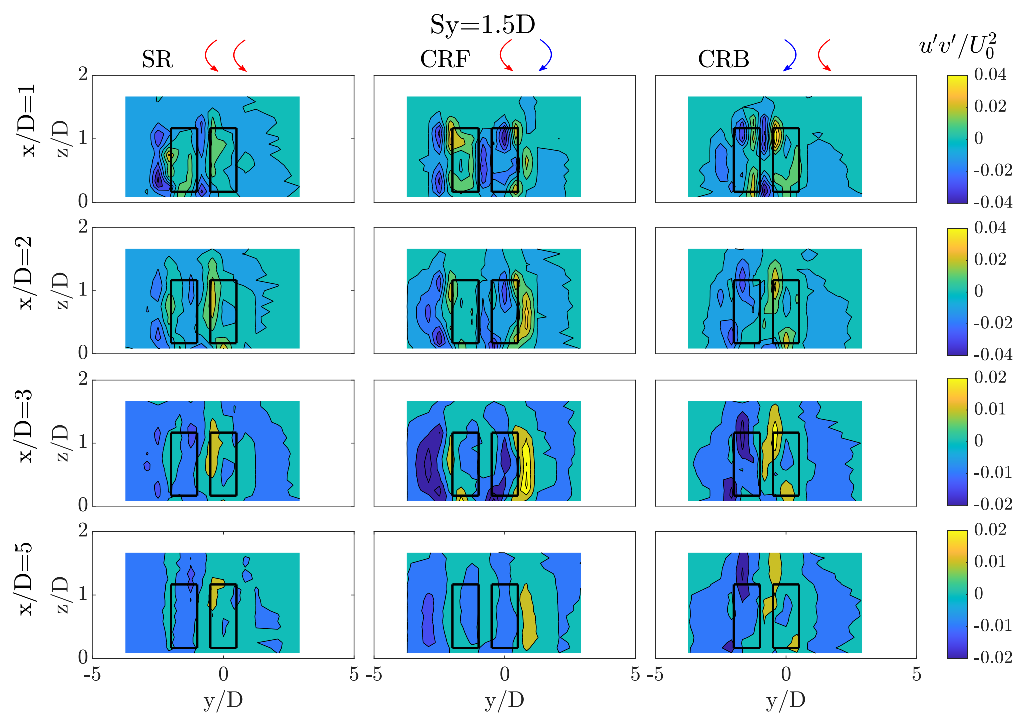

Figure 13: Cross section contours of $\overline{u'v'}/U_0^2$ at downstream locations of $x/D = 1$, 2, 3, and 5 for the co-rotating (SR–1.5; left), counter-rotating forward (CRF–1.5; middle), and counter-rotating backward (CRB–1.5; right) with $S_y/D = 1.5$. The solid black rectangles represent the perimeter of the turbine's rotor. The flume's centreline is located at $y/D = 0$. Legend scale is adjusted for different streamwise locations (x/D) to ease depiction of hydrodynamic features.

Reynolds shear stresses $\overline{u'v'}/U_0^2$ and $\overline{u'w'}/U_0^2$ are presented in Figures 13 and 14, respectively, for all $S_y/D = 1.5$ twin-VAT cases. Peak $\overline{u'v'}/U_0^2$ magnitudes were ob-

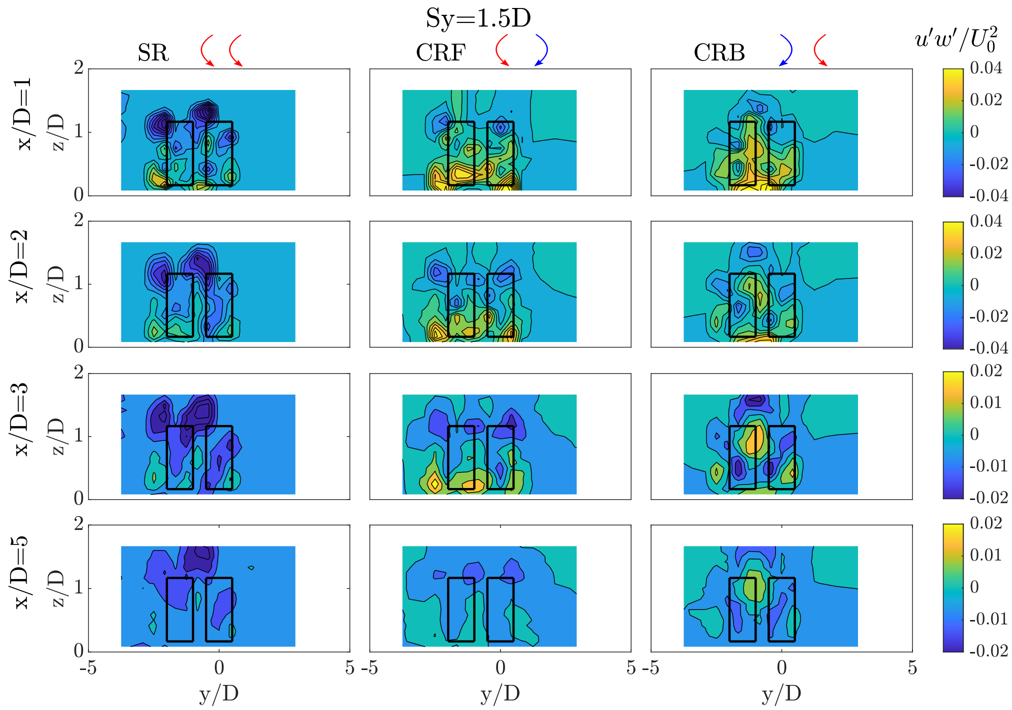

Figure 14: Cross section contours of $\overline{u'w'}/U_0^2$ at downstream locations of $x/D = 1$, 2, 3, and 5 for the SR–1.5 (left), CRF–1.5 (middle), and CRB–1.5 (right) cases. The solid black rectangles represent the perimeter of the turbine's rotor. The flume's centreline is located at $y/D = 0$. Legend scale is adjusted for different streamwise locations (x/D) to ease depiction of hydrodynamic features.

served on the periphery of the swept areas of each turbine, indicative of turbulent momentum exchange and where vortices are generated. These are clearly observed for the CRF–1.5 case even up to $x/D = 5.0$. Similar to the ST case, vertical Reynolds shear stresses $\overline{u'w'}/U_0^2$ were mostly negative on the upper half of the turbines as turbulent momentum entrained downwards into the wake region, and positive on the lower half; with the exception of CRB–1.5 in which the mixing of vortical structures from each of the turbine rotors showed a different pattern suggesting that the turbulent wake flow is more complex for this setup. Tip vortices were also present, triggering high shear stress levels around the top tips of the blades in the near wake ($x/D \leq 2$).

4.4. Wake recovery

The integral change of the wake in the downstream direction was estimated in terms of the cross-sectional average of the streamwise velocity and turbulence intensity. These were approximated by integrating the measured quantities at the ADV locations within the turbine area for ST case ($0.5 \leq y/D \leq 0.5$) and the region spanning both VATs for the twin setups ($S_y/D = 1.5$: $0.5 \leq y/D \leq 2$, $S_y/D = 2.0$: $0.5 \leq y/D \leq 2.5$). In the vertical, only those points within the turbine area were considered. The spatial-averaging operation is denoted as $\langle\cdot\rangle$ and results of $(\langle\overline{u}\rangle/U_0)$ and $(\langle u'\rangle/U_0)$ are provided in Figures 15 and 16 for the ST and six twin-VAT cases comparing rotational direction and lateral spacing, respectively.

Immediately downstream of the turbines ($x/D = 1$), the cross-sectional mean velocity recovery was observed to exceed values of $\langle\overline{u}\rangle/U_0 \geq 50\%$ for all configurations, especially for CRF (counter-rotating forward) configurations which attained the highest initial wake velocity. Larger intra-turbine spacing consistently enhanced wake recovery due to a higher momentum flowing through the bypass region, e.g., in the case of CRF–2.0, $\langle\overline{u}\rangle/U_0$ fully recovered the bulk velocity value at $x/D = 5$, while for CRF–1.5 this was at approximately $x/D = 8$. Vergaerde et al. [17] adopted an inter-turbine spacing of $S_y/D = 1.3$ reporting a wake recovery of 75% at $x/D = 5.2$.

Figure 16 indicates that rotational direction plays a more important role than lateral spacing shown in Figure 15 for the current values of S_y. In comparison to the single turbine case, CRF configurations featured the largest kinetic energy in the wake region due to a higher initial wake velocity, even exceeding the velocities from the single turbine wake. CRB setups followed a similar wake velocity evolution over the wake length as the single turbine but with full wake recovery attained at 8 and 10 diameters downstream, respectively. The slowest wake recovery was found for SR cases that achieved velocities of $\langle\overline{u}\rangle/U_0 \geq 80\%$ at $x/D = 10$ despite featuring larger velocities than the single turbine case at $x/D = 1$.

In terms of wake unsteadiness, the highest turbulence intensity values $(\langle u'\rangle/U_0)$ were found for both CRB (counter-rotating backward) cases as a consequence of the large interaction between both wakes at all downstream locations, while the lowest turbulence intensities were found in the case of CRF–2.0 due to the wider inter-turbine spacing that minimised the interplay between turbulent wakes. Some variability in the spatially-averaged turbulence intensity is observed at $x/D = 1$, 1.5 and 2 for configurations with S_y/D=2.0, agreeing with the contours shown in Figure 20. In all cases, free-stream values of $\langle u'\rangle/U_0$ were reached at approximately $x/D = 10$.

The rate of wake recovery of the seven configurations is presented in Figure 17, showing the spatially-averaged velocity deficit $(\Delta\langle\overline{u}\rangle)$ and decay slopes of -1/3, -1/2 and -2/3. Classic shear-flow theory states that for self-similar axisymmetric and planar wakes the velocity deficit decay should be proportional to $x^{-2/3}$ and $x^{-1/2}$,

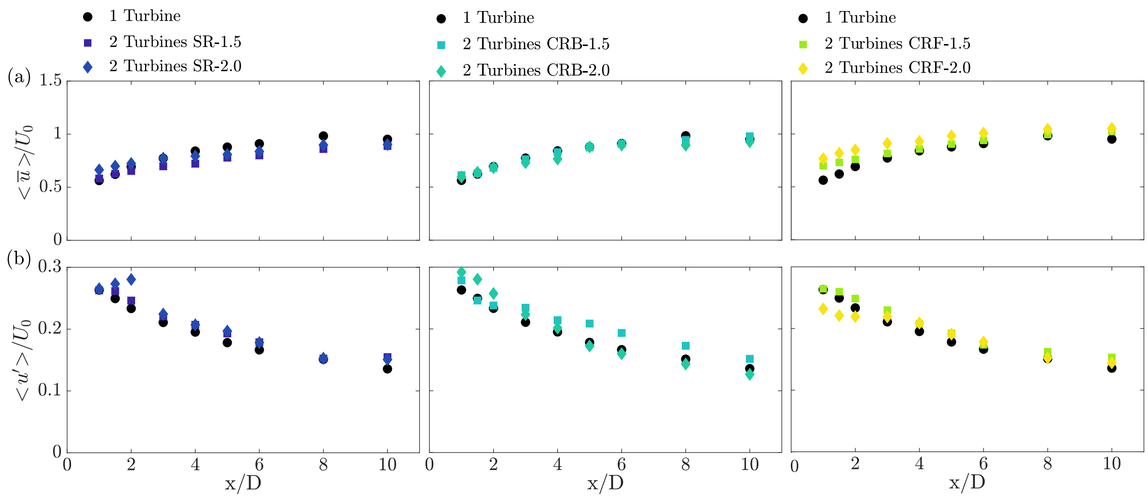

Figure 15: Comparison of the lateral spacing impact for the three rotational directions with values of spatially-averaged (a) mean streamwise velocity $\langle\overline{u}\rangle$, and (b) turbulent intensity $\langle u'\rangle$, normalised by U_0 at all measured locations in downstream direction.

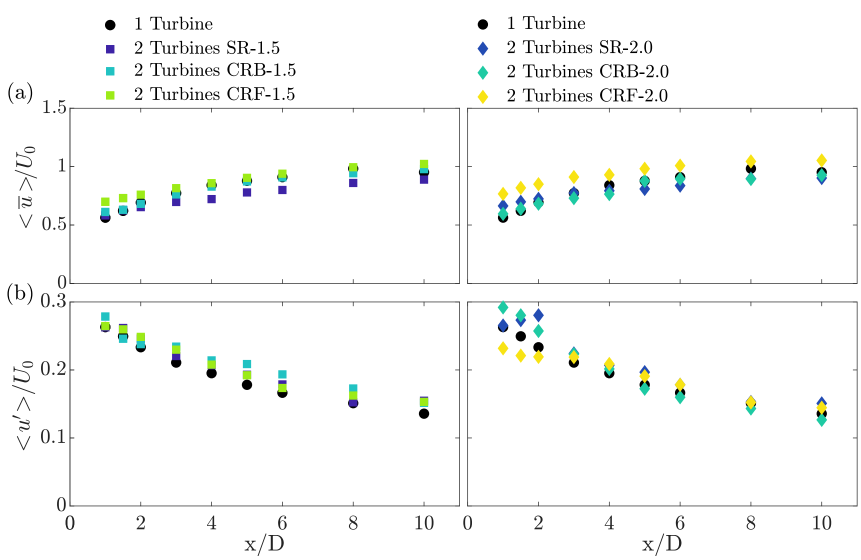

Figure 16: Comparison of the rotational direction for the two lateral spacing values with values of spatially-averaged (a) mean streamwise velocity $\langle\overline{u}\rangle$, and (b) turbulent intensity $\langle u'\rangle$, normalised by U_0 at all measured locations in downstream direction.

respectively [35]. Here, whilst VAT wakes did not attain self-similarity within the measured range of $1 \leq x/D \leq 10$, the decay rates were between -1/3 and -2/3 for all cases. The single turbine (ST) and both CRB cases followed a -1/2 slope over the measured wake length. In contrast, the SR cases showed an initial slope approx. equal to -1/3 until $x/D = 4$–5 downstream when the slope increases and is closer to a -1/2 decay. CRF setups featured the slowest decay rates of -1/3 over the wake length, although these configurations showed the lowest velocity deficit at the wake onset.

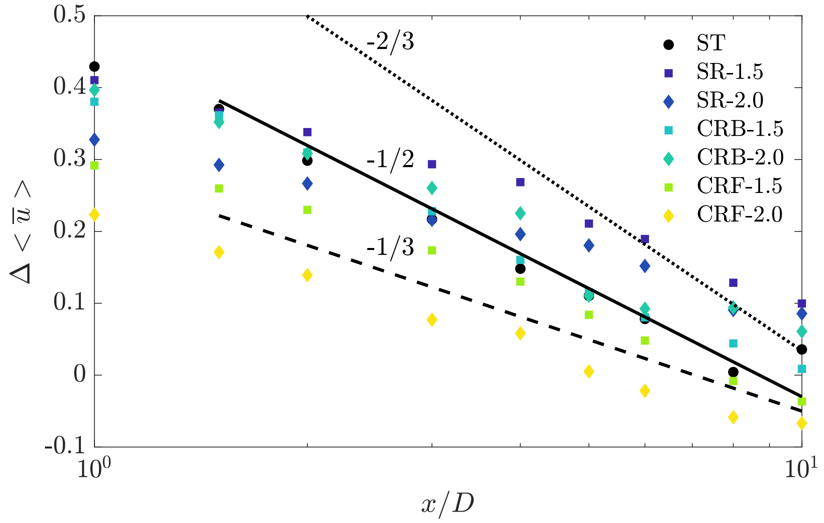

Figure 17: Wake recovery rate obtained from the spatially-averaged velocity deficit $\Delta\langle\overline{u}\rangle$ in semi-log scale for the seven cases. Straight, dashed and dotted lines represent the -1/2, -1/3 and -2/3 slopes.

Overall the results presented suggest that a lateral spacing of, at least, $2D$ should be considered with a counter-rotating forwards (CRF) configuration to enhance wake recovery when designing arrays of VATs with a minimum of two turbines per row to minimise detrimental wake effects. Further research, however, will be required to identify the optimal lateral turbine spacing. Moreover, configurations with a lateral spacing of $2D$ attained a faster wake recovery and experienced lower turbulence intensity. This suggests that in arrays with greater inter-turbine spacing, the production of turbulent kinetic energy is enhanced as a result of the destruction of the kinetic energy of the mean flow that delays the momentum recovery rate. As per the rotational direction of the twin-turbines, counter-rotating forwards leads to the largest velocities in the wake region and thus there is a larger kinetic energy to be extracted by secondary rows.

4.5. Wake superposition

To provide further insights into the interaction between individual wakes in the twin configurations, the streamwise velocity deficit ($\Delta\overline{u} = 1 - \overline{u}/U_0$) of the wake from the ST case is superimposed using linear ($\Delta\overline{u}_{lin} = \Delta\overline{u}_{T_1} + \Delta\overline{u}_{T_2}$) and quadratic ($\Delta\overline{u}_{quad} = [(\Delta\overline{u}_{T_1})^2 + (\Delta\overline{u}_{T_2})^2]^{0.5}$) superposition and compared to the actual measured values obtained for the six twin configurations.

Velocity deficit results at turbine mid-height ($z/D = 0.67$) for five downstream locations for the SR–1.5 and SR–2.0 are shown in Figure 18, together with the linear and quadratic wake superposition predictions, and values of the ST case. Within the near wake region ($x/D \leq 2$), both wakes have not yet interacted with each other, resulting in a good agreement from their individual superposition. Further downstream from the turbines ($x/D \geq 4$), the velocity deficit in the wake of T_2 for SR–1.5 was slightly underestimated whilst at $y/D \approx 1.0$ the linear model provides a better fit than the quadratic superposition which overpredicts $\Delta\overline{u}$. The observed small deviation between the superimposed wakes and actual measurements indicates that cumulative flow effects on the evolution and merging of interacting twin-VAT wakes are well represented with simple superposition techniques at all locations.

The root-mean-square (rms) error of the spatially-averaged mean streamwise velocity $\langle\overline{u}\rangle$ between the linear and quadratic superposition predictions and measured experimental results were computed at each streamwise location for the six twin-VAT configurations (Figure 19). Independent of the lateral spacing, a lower rms error was found for SR cases, indicating that the developed combined wakes have reduced non-linear interactions, allowing the superposition models to provide good predictions of the velocity field. However, for CRB (counter-rotating backward) setups, the superposition methods show a larger sensitivity to the lateral spacing (S_y/D) with rms values for CRB–1.5 being higher than those for CRB–2.0 over the entire wake length. In the latter case, the turbine wakes are closer and thus there is a higher degree of interaction between them.

Considering the CRF cases, the accuracy of the superposition models remains almost unchanged for the two intra-turbine spacing values. In comparison, rms values of spatially averaged velocity reduced for $S_y/D = 2.0$ due to a wider spacing between devices and thus a limited wake interaction (Figure 11). Overall, the linear approach provides lower rms errors than the quadratic superposition when predicting the mean velocity field.

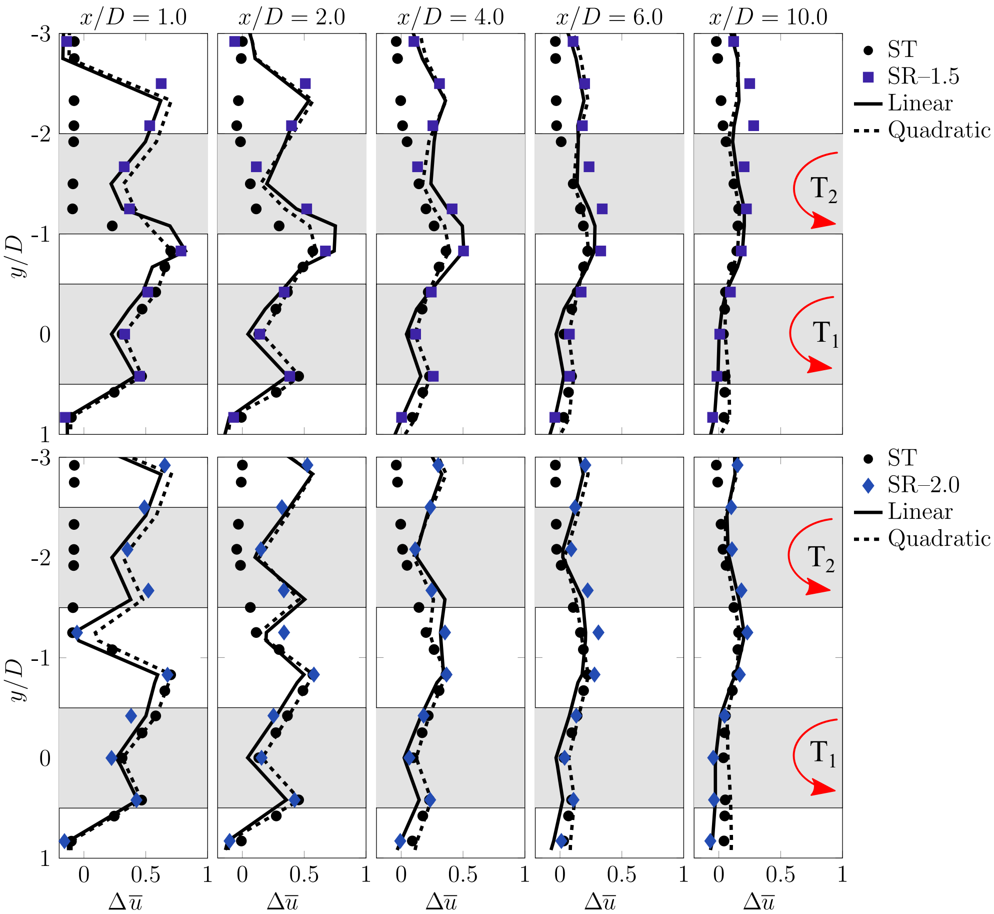

Figure 18: Results of velocity deficit ($\Delta\overline{u}$) of the SR–1.5 (top) SR–2.0 (bottom) cases with the calculation from the linear and quadratic superposition models. ST case data is included for convenience. Shaded areas denote the projected turbine's rotor swept area. The centreline of the flume is located at y/D=0.

5. Conclusion

The evolution and interaction between the wakes of adjacent Vertical Axis Turbines (VATs) deployed in twin configurations has been experimentally studied by means of acoustic Doppler velocimeter (ADV) measurements. A standalone and six twin-VAT setups were tested, including shaft-to-shaft spacings (S_y) of 1.5 and 2.0 turbine diameters (D) with the devices rotating in the same and in opposite directions. The results presented show that the wake evolution was more sensitive to the rotational direction of the VATs than their lateral spacing for the range of S_y

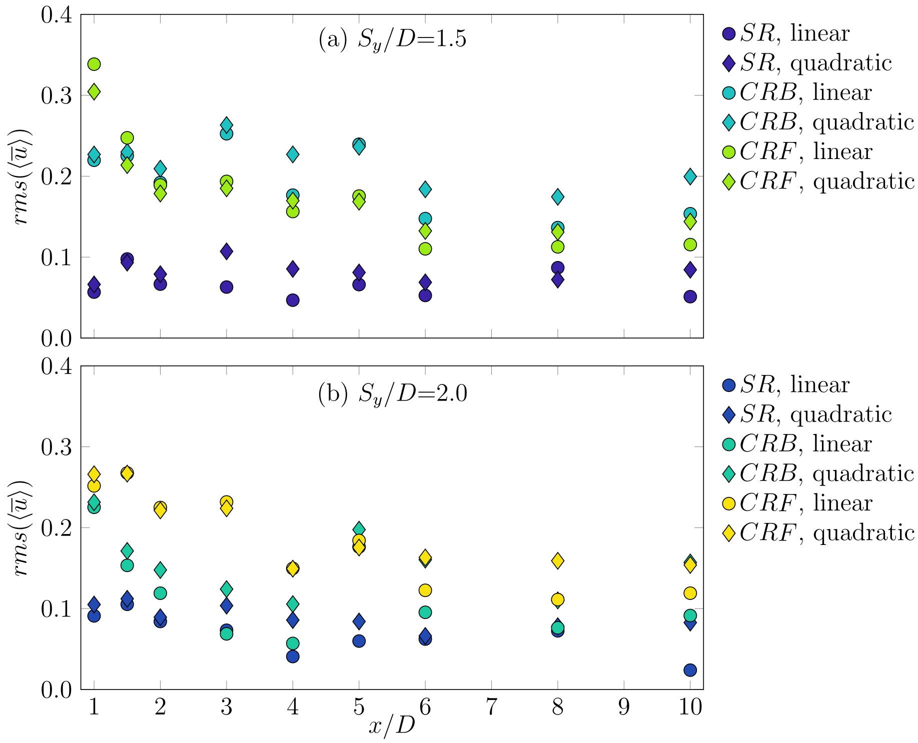

Figure 19: Root-mean-square (rms) error in the prediction of the spatially averaged mean streamwise velocity $\langle\overline{u}\rangle$ adopting linear and quadratic superposition methods for the twin-turbine cases with $S_y/D = 1.5$ (a) and 2.0 (b).

values adopted. When VATs rotated in the same direction (SR cases), the wake region notably expanded in the lateral and vertical directions. In the counter-rotating forwards setups (CRF, i.e., turbine blades move along with the flow in the bypass region), the highest momentum deficit was found in the downstroke regions on the outskirts of the wake, preventing the wakes from merging and therefore, allowing larger velocities in the wake. In the counter-rotating backwards cases (CRB, i.e., blades move against the flow in the bypass region), the low-velocity regions merged immediately downstream of the turbines, generating a single wake that was relatively narrow in the lateral direction but expanded over the whole water column after 3 or $5D$ downstream of the turbines depending on whether the intra-turbine spacings was $1.5D$ or $2.0D$, respectively. Similar distribution patterns were observed in the turbulent kinetic energy and Reynolds shear stresses.

Cross-sectional averaged values of mean velocity and turbulence intensity outlined that cases with turbines rotating in a counter-rotating forward (CRF) sense achieved the highest momentum in the wake. This was specially noticeable for the CRF–2.0 configuration in which the cross-sectional mean velocity reached the bulk velocity value (U_0) at $5D$ downstream, a distance noticeably shorter than the $8D$ at which the single turbine attained full wake recovery. The rate of momentum deficit decay was slowest for the latter CRF cases, being proportional to $(x/D)^{-1/3}$, whilst for the CRB cases and the single turbine featured similar wake velocities with a faster recovery rate close to $(x/D)^{-1/2}$. Conversely, SR setups achieved the lowest velocities in the wake, with a value of $90\%U_0$ at the furthest measured location of $x/D = 10$, with the velocity deficit recovering at an approx. rate of $(x/D)^{-1/3}$ until 4–$5D$ after which the decay accelerated with a -1/2 slope.

The momentum recovery was enhanced and turbulence intensity decreased with increasing intra-turbine spacings, i.e., adopting $S_y/D = 2$, suggesting that greater turbine spacings may be beneficial when designing multi-row twin-VAT arrays. Further research, however, will be required to identify the optimal lateral distance between turbines that maximises installed power density per unit land, i.e., taking into account reduced wake effects to enhance the performance of downstream turbines while allowing the twin-turbines to increase device energy yield due to synergistic blockage effects.

Despite the complexity of the wake dynamics, adopting a linear or quadratic superposition of a single turbine wake in the horizontal plane appeared to yield good results when compared to experimentally measured mean velocity values. In terms of root-mean-square errors, these were higher for turbines rotating in a counter-rotating manner as the dynamics of the interacting wakes might result in more non-linear effects.

This study provides new insights into the wake characteristics behind twin-VAT arrays and informs the design of future multi-row arrays of VATs with minimised wake-turbine interactions. The measured wakes suggest that a lateral spacing of $2D$ with a counter-rotating forward (CRF) setup would allow to adopt a streamwise spacing between rows of $5D$ so that secondary rows can harness kinetic energy efficiently. On the other hand, adopting configurations with turbines rotating in the counter-rotating backwards (CRB) and same rotation (SR) sense would require a wider streamwise inter-row spacing of, at least, $10D$ unless the lateral turbine spacing is increased which, however, would decrease the installed power density capacity.

Acknowledgement

This research was financially supported using seed funding from Cardiff University's GCRF QR Funding from the Higher Education Funding Council for Wales, under the project "HEFCW GCRF Small Project SP111: A new technology of fish-friendly river turbines to provide renewable energy to impoverished isolated communities". In addition, SM was funded as part of the Water Informatics Science and Engineering Centre for Doctoral Training (WISE CDT) under grant EP/L016214/1 from the Engineering and Physical Science Research Council (EPSRC). The authors are grateful to Dr Aldo Benavides, Dr Carlos Duque and Maxime Lacennec for the fruitful conversations about this research, and Paul Leach for his invaluable support to build the turbine prototypes and technical assistance during the measurements. Data underpinning the results presented here can be found in the Cardiff University data catalogue: `http://doi.org/10.17035/d.2021.0134567672`. Comments from the Editor and three anonymous reviewers are greatly appreciated.

6. Appendix

Here, the results obtained for the twin-VAT configurations with $S_y/D = 2.0$ are presented in terms of turbulent kinetic energy (Figure 20), horizontal (Figure 21) and vertical (Figure 22) Reynolds shear stresses. In these figures, the rectangular outline indicates the swept area of the turbines.

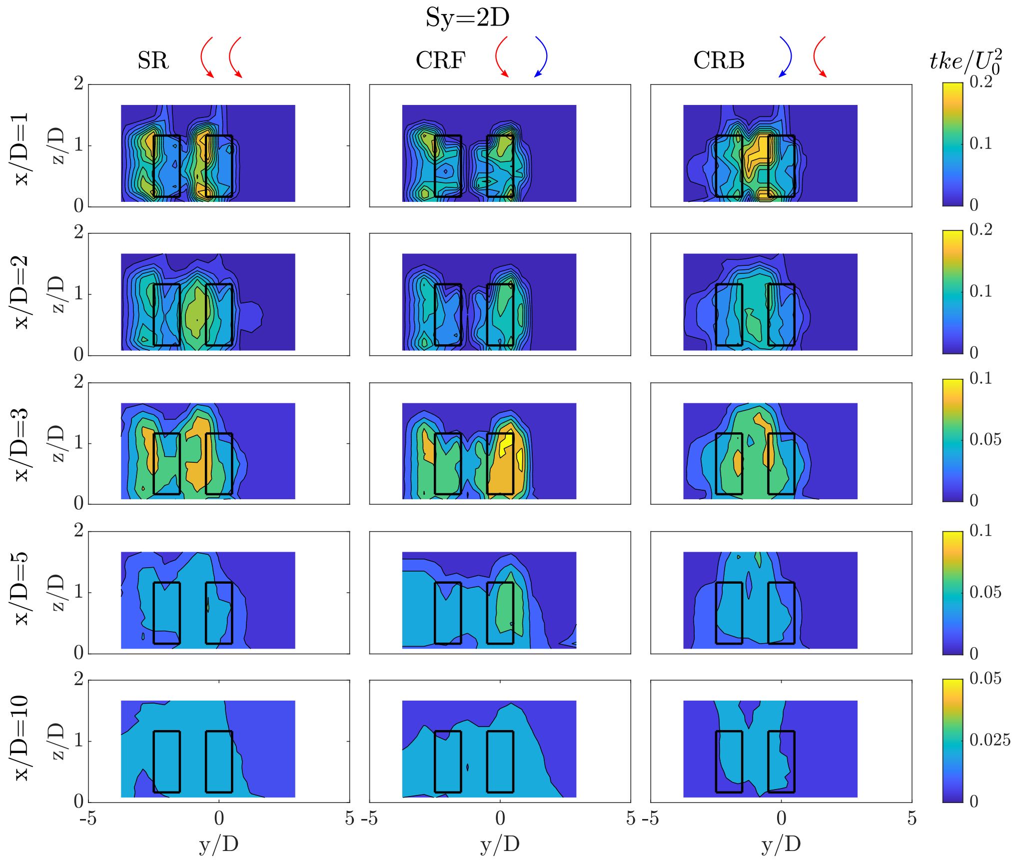

Figure 20: Cross section contours of tke/U_0^2 at downstream locations of $x/D = 1$, 2, 3, and 5 for the SR–2.0, CRF–2.0 and CRB–2.0. The solid black rectangles represent the perimeter of the turbine's rotor. The flume's centreline is located at $y/D = 0$. Legend scale is adjusted for different streamwise locations (x/D) to ease depiction of hydrodynamic features.

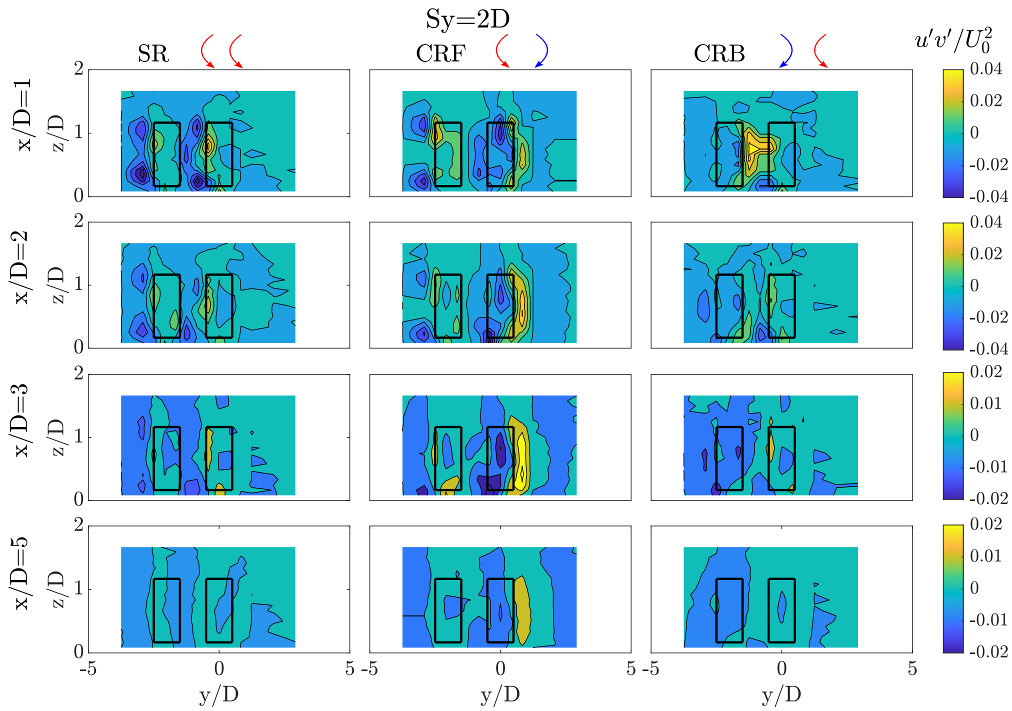

Figure 21: Cross section contours of $\overline{u'v'}/U_0^2$ at downstream locations of x/D = 1, 2, 3, and 5 for the SR–2.0, CRF–2.0 and CRB–2.0. The solid black rectangles represent the perimeter of the turbine's rotor. The flume's centreline is located at $y/D = 0$. Legend scale is adjusted for different streamwise locations (x/D) to ease depiction of hydrodynamic features.

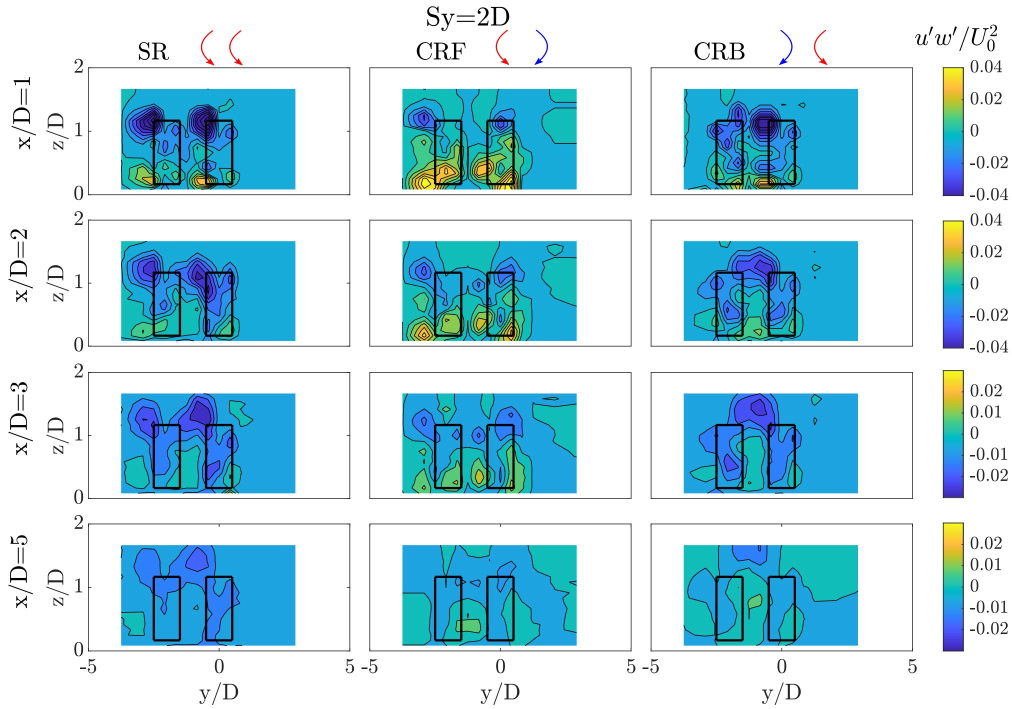

Figure 22: Cross section contours of $\overline{u'w'}/U_0^2$ at downstream locations of x/D = 1, 2, 3, and 5 for the SR–2.0, CRF–2.0 and CRB–2.0. The solid black rectangles represent the perimeter of the turbine's rotor. The flume's centreline is located at $y/D = 0$. Legend scale is adjusted for different streamwise locations (x/D) to ease depiction of hydrodynamic features.

References

[1] REN21, Renewables 2020 Global Status Report, 2020.

[2] T. Abbasi, S. A. Abbasi, Small hydro and the environmental implications of its extensive utilization, Renewable and Sustainable Energy Reviews 15 (2011) 2134–2143. `doi:10.1016/j.rser.2010.11.050`.

[3] T. H. Bakken, H. sundt, A. Ruud, A. Harby Development of small versus large hydropower in Norway - comparison of environmental impacts, Energy Procedia 20 (2012) 185–199. `doi:10.1016/j.egypro.2012.03.019`.

[4] M. Kinzel, Q. Mulligan, J. O. Dabiri, Energy exchange in an array of vertical-axis wind turbines, Journal of Turbulence 14 (38) (2012) 1–13. `doi:10.1080/14685248.2012.712698`.

[5] J. O. Dabiri, Potential order-of-magnitude enhancement of wind farm power density via counter-rotating vertical-axis wind turbine arrays, Journal of Renewable and Sustainable Energy 3 (4). doi:10.1063/1.3608170.

[6] M. J. Khan, G. Bhuyan, M. T. Iqbal, J. E. Quaicoe, Hydrokinetic energy conversion systems and assessment of horizontal and vertical axis turbines for river and tidal applications: A technology status review, Applied Energy 86 (10) (2009) 1823–1835. doi:10.1016/j.apenergy.2009.02.017.

[7] T. Castro-Santos, A. Haro, Survival and Behavioral Effects of Exposure to a Hydrokinetic Turbine on Juvenile Atlantic Salmon and Adult American Shad, Estuaries and Coasts 38 (1) (2015) 203–214. doi:10.1007/s12237-013-9680-6.

[8] M. Kinzel, D. B. Araya, J. O. Dabiri, Turbulence in vertical axis wind turbine canopies, Physics of Fluids 27 (115102) (2015) 1–18. doi:10.1063/1.4935111.

[9] G. Brochier, P. Fraunie, C. Beguier, I. Paraschivoiu, Water channel experiments of dynamic stall on darrieus wind turbine blades, Journal of Propulsion and Power 2 (5) (1986) 445–449. doi:10.2514/3.22927.

[10] P. Bachant, M. Wosnik, Performance measurements of cylindrical- and spherical-helical cross-flow marine hydrokinetic turbines, with estimates of energy efficiency, Renewable Energy 74 (2015) 318–325. doi:10.1016/j.renene.2014.07.049.

[11] D. B. Araya, T. Colonius, J. O. Dabiri, Transition to bluff-body dynamics in the wake of vertical-axis wind turbines, Journal of Fluid Mechanics 813 (2017) 346–381. doi:10.1017/jfm.2016.862.

[12] P. Ouro, S. Runge, Q. Luo, T. Stoesser, Three-dimensionality of the wake recovery behind a vertical axis turbine, Renewable Energy 133 (2019) 1066–1077. doi:10.1016/j.renene.2018.10.111.

[13] B. Strom, B. Polagye, S. Brunton, Intracycle angular velocity control of cross-flow turbines, Nature Energy 2 (2017) 1–9 http://dx.doi.org/10.1038/nenergy.2017.103.

[14] G. Tescione, D. Ragni, C. He, C. J. Simão Ferreira, G. J. van Bussel, Near wake flow analysis of a vertical axis wind turbine by stereoscopic particle image velocimetry, Renewable Energy 70 (2014) 47–61. doi:10.1016/j.renene.2014.02.042.

[15] H. Kadum, S. Friedman, E.H. Camp, R.B. Cal, Development and scaling of a vertical axis wind turbine wake, Journal of Wind Engineering and Industrial Aerodynamics 174 (2018) 303–311. doi:10.1016/j.jweia.2018.01.004.

[16] V. F. Rolin, F. Porté-Agel, Experimental investigation of vertical-axis wind-turbine wakes in boundary layer flow, Renewable Energy 118 (2018) 1–13. doi:10.1016/j.renene.2017.10.105.

[17] A. Vergaerde, T. De Troyer, S. Muggiasca, I. Bayati, M. Belloli, J. Kluczewska-Bordier, N. Parneix, F. Silvert, M. C. Runacres, Experimental characterisation of the wake behind paired vertical-axis wind turbines, Journal of Wind Engineering & Industrial Aerodynamics 206 (104353) (2020) 1–13. doi:10.1016/j.jweia.2020.104353

[18] S. Shamsoddin, F. Porté-Age, A large-eddy simulation study of vertical axis wind turbine wakes in the atmospheric boundary layer, Energies 9 (5) (2016) 1–23. doi:10.3390/en9050366.

[19] H. F. Lam, H. Y. Peng, Study of wake characteristics of a vertical axis wind turbine by two- and three-dimensional computational fluid dynamics simulations, Renewable Energy 90 (2016) 386–398. doi:10.1016/j.renene.2016.01.011.

[20] A. Posa, C. M. Parker, M. C. Leftwich, E. Balaras, Wake structure of a single vertical axis wind turbine, International Journal of Heat and Fluid Flow 61 (2016) 75–84. doi:10.1016/j.ijheatfluidflow.2016.02.002.

[21] M. Abkar, J. O. Dabiri, Self-similarity and flow characteristics of vertical-axis wind turbine wakes: an LES study, Journal of Turbulence 18 (4) (2017) 373–389. doi:10.1080/14685248.2017.1284327.

[22] P. Ouro, T. Stoesser, An immersed boundary-based large-eddy simulation approach to predict the performance of vertical axis tidal turbines, Comput. Fluids 152 (2017) 74–87. doi:10.1016/j.compfluid.2017.04.003.

[23] A. Posa, Dependence of the wake recovery downstream of a vertical axis wind turbine on its dynamic solidity, Journal of Wind Engineering & Industrial Aerodynamics 202 (2020) 104212. doi:10.1016/j.jweia.2020.104212.

[24] S.H. Han, J.S. Park, K.S. Lee, W.S. Park, J.H. Yi, Evaluation of vertical axis turbine characteristics for tidal current power plant based on in situ experiment, Ocean Engineering 65 (2013) 83–89. doi:10.1016/j.oceaneng.2013.03.005.

[25] P. Ouro, M. Lazennec, Theoretical modelling of the three-dimensional wake of vertical axis turbines, Flow 1: E3 (2021) doi:10.1016/10.1017/flo.2021.4.

[26] H. Su, H. Meng, T. Qu, L. Lei, Wind tunnel experiment on the influence of array configuration on the power performance of vertical axis wind turbines, Energy Conversion and Management 241 (2021) 114299 http://dx.doi.org/10.1016/j.enconman.2021.114299.

[27] A. Posa, Wake characterization of coupled configurations of vertical axis wind turbines using Large Eddy Simulation, International Journal of Heat and Fluid Flow 75 (2019) 27–43. doi:10.1016/j.ijheatfluidflow.2018.11.008.

[28] S. Zanforlin, T. Nishino, Fluid dynamic mechanisms of enhanced power generation by closely spaced vertical axis wind turbines, Renewable Energy 99 (2016) 1213–1226. doi:10.1016/j.renene.2016.08.015.

[29] H. F. Lam, H. Y. Peng, Measurements of the wake characteristics of co- and counter-rotating twin H-rotor vertical axis wind turbines, Energy 131 (2017) 13–26. doi:10.1016/j.energy.2017.05.015.

[30] S. Sahebzadeh, A. Rezaeiha, H. Montazeri, Towards optimal layout design of vertical-axis wind-turbine farms: Double rotor arrangements, Energy Conversion and Management 226 (2020) 113527 http://dx.doi.org/10.1016/j.enconman.2020.113527.

[31] Y. Jiang, P. Zhao, T. Stoesser, K. Wang, L. Zou, Experimental and numerical investigation of twin vertical axis wind turbines with a deflector, Energy Conversion and Management 209 (2020) 112588. doi:10.1016/j.enconman.2020.112588.

[32] N. Mori, T. Suzuki, S. Kakuno, Noise of acoustic Doppler velocimeter data in bubbly flows, Journal of Engineering Mechanics 133 (1) (2007) 122–125. doi:10.1061/(ASCE)0733-9399(2007)133:1(122).

[33] N. Mori, Despiking, MATLAB CentralFile Exchange. Retrieved February 24, 2021.

[34] T. Stoesser, R. McSherry, B. Fraga, Secondary currents and turbulence over a non-uniformly roughened open-channel bed, Water 7 (9) (2015) 4896–4913. doi:10.3390/w7094896.

[35] H. Tennekes, JL. Lumley, A first couse in turbulence, The MIT Press; 1972.